Soft Matter

PAPER

View Article Online
View Journal | View Issue

Cite this: *Soft Matter*, 2021, **17**, 6728

On the relationship between cutting and tearing in soft elastic solids†

Bingyang Zhang and Shelby B. Hutchens *

Received 8th April 2021,
Accepted 14th June 2021

DOI: 10.1039/d1sm00527h

rsc.li/soft-matter-journal

Unique observations of cutting energy in silicone elastomers motivate a picture of soft fracture that qualitatively and quantitatively links far-field tearing with push cutting for the first time. For blades of decreasing tip radii, the cutting energy decreases until it reaches a plateau that suggests a threshold for failure. A super-molecular damage zone, necessary for new surface creation, is defined using the tip radius at the onset of this threshold. Modifying the classic Lake–Thomas theory, in which failure occurs within a molecular plane, to this super-molecular zone provides order-of-magnitude agreement with the cutting energy threshold. Together, the threshold fracture energy and damage length scale define criteria for failure that, when implemented in finite element simulation, quantitatively reproduce the increase in cutting energy with increasing blade radius outside of the plateau. The rate of increase depends on the constitutive response of the material, with more neo-Hookean solids requiring a larger failure force per incremental increase in blade radius as observed experimentally. This combination of a geometry-independent failure threshold (from the cutting energy plateau) and a need to account for the role of material deformability in the stress concentration found at the crack tip (from the rate of cutting energy increase with blade radius) align with the discovery of a new dimensionless group. This new parameter proportionally maps cutting energy to the energy required to tear a sample under far-field loading conditions by using ultimate properties obtained in uniaxial tension.

1 Introduction

Measurement of a material's fracture energy aims to provide a universal window into its failure behavior under a wide range of loading conditions. Such universality is true for many brittle or elastic–plastic materials that exhibit small elastic deformations. In contrast, soft solids' ability to undergo large deformations and exhibit a wide variety of nonlinearities, internal damage accumulation mechanisms, and highly time-dependent responses can make generalizations of fracture energy measured under one condition inapplicable to another. This is true of the comparison between cutting and tearing.

While modelers and experimentalists alike have often assumed directly or indirectly that a strain energy release rate measured from cutting tests directly quantifies that which would be measured in tearing, this assumption does not hold for elastomeric materials.[1–3] Unless the radius of the blade is sufficiently small, even measurements obtained during cutting will vary with the tip radius of the cutting implement.[4] A similar behavior for blade angle may exist,[5,6] though it is as yet unexplored. Here, we document the discrepancy between cutting and tearing energy (Fig. 1a) for highly elastic materials using push-cutting energy determined *via* a Y-shaped test geometry[1,4] that avoids friction and allows for steady-state crack propagation (Fig. 1b). Cutting, in which a small crack tip radius is dictated by the blade geometry, differs from pure shear tearing, in which crack blunting occurs. However, both geometries are predominantly Mode I and, as we will show, exhibit a similar hierarchy of the length scales that characterize their response (Fig. 1c–e). In soft elastic materials, the onset of failure is regulated by both a material's deformability, which accommodates the loading conditions, and its local, intrinsic threshold for rupture.[7–10] Observations of the blade-radius-dependence of cutting provides information on both of these characteristics. At low radii, the cutting energy reaches a lower limit that defines a threshold, highly-deformed volume required for new surface creation. At larger radii, we use these failure criteria, combined with material constitutive response to quantitatively predict the sensitivity of cutting energy to increases in radius. Additionally, both deformability and failure onset play a role in a new dimensionless parameter discovered *via* scaling analysis. This parameter is based on ultimate properties measured under uniaxial tension and enables the direct, proportional mapping of cutting energy to tearing energy in the highly elastic, minimally hysteretic silicones presented here (Fig. 1a, inset).

Mechanical Science and Engineering, University of Illinois Urbana-Champaign, Urbana, IL, USA. E-mail: hutchs@illinois.edu; Tel: +1 217 300 0412

† Electronic supplementary information (ESI) available: Supplementary documentation. See DOI: 10.1039/d1sm00527h

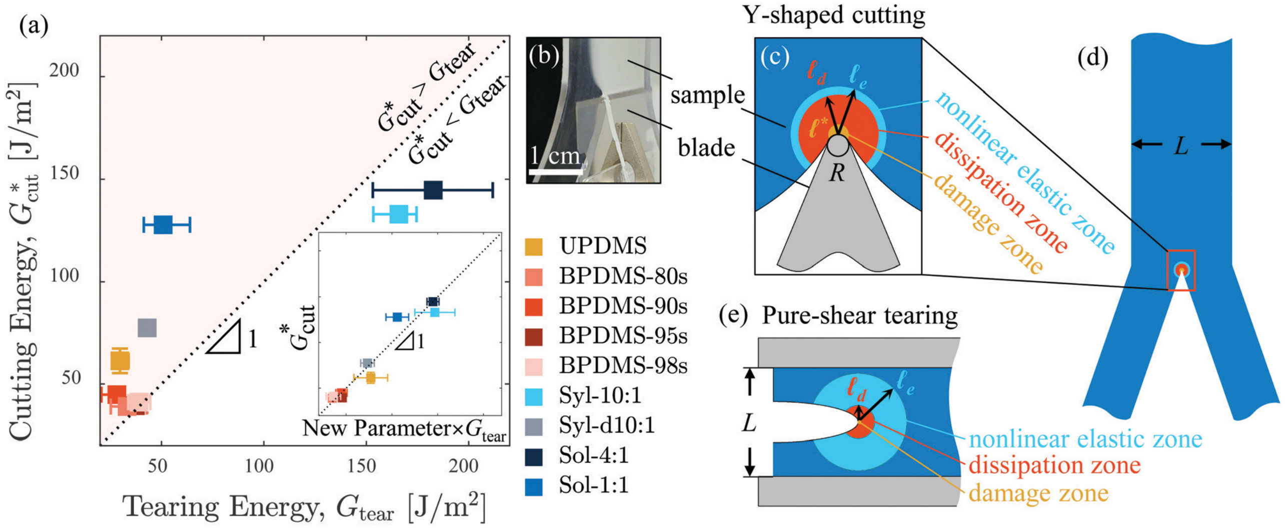

Fig. 1 Y-shaped cutting *versus* pure-shear tearing. (a) Failure energies determined in cutting G^*_{cut} do not scale proportionally with those measuring in tearing G_{tear}. The dotted line illustrates proportionality, $G^*_{\mathrm{cut}} = G_{\mathrm{tear}}$. Inset: When a dimensionless equivalency parameter is multiplied by G_{tear}, failure energies collapse to proportional relationship. (b) A close-up image of the cut region showing the length scale of a Y-shaped sample relative to the blade. (c) The region around the crack tip in cutting is divided into three zones with length scales corresponding to the onset of nonlinear elasticity ℓ_{e}, onset of dissipation effects ℓ_{d}, and the threshold required for surface creation ℓ^*. These zones satisfy small-scale yield for the macroscopic cutting sample of size L shown in (d). (e) ℓ_{e} and ℓ_{d} are significantly larger under far-field tearing for a sample of equal size L.

Elastomers exhibiting a larger viscous response and/or hysteresis-producing damage mechanisms (*e.g.*, Mullins effect[11] or double-network structure[12]) may not be described without further modification of the approach we employ. This may be due to the fact the measured fracture toughness G of a material is thought to be comprised of both a threshold value associated with new surface creation and a dissipation component in the bulk, $G = G_{\mathrm{t}} + G_{\mathrm{d}}$, respectively. The dissipation energy contribution can be amplified in soft materials by crack tip blunting,[13] which gives rise to larger highly deformed volumes during tearing.[8,9] As we will show, the highly deformed volume in cutting is significantly smaller and subject to different loading conditions. When the energy dissipated within that zone is large (due to viscous interactions or damage accumulation), it contributes markedly to the measured failure energy. When energy dissipation is minimal, as is the case for the materials tested here, we find that tearing and cutting may be related. Understanding the contribution of the former viscous and dissipative effects likely requires stress-gradient-dependent damage and viscosity models that are outside the purview of the current work.

Although dissipative effects are minimal, a dissipation zone still exists (illustrated schematically in Fig. 1c–e). The length scales defining this zone and the onset of nonlinearity under far-field loading conditions (*i.e.*, tearing) have been recently described by Long *et al.*[9] The interplay of these length scales are found to characterize the type of failure typically observed in elastomers, namely soft, ductile failure. The length scale for the onset of material nonlinearity, also known as the elastocohesive length,[8] scales as $\ell_{\mathrm{e}} \sim \Gamma/E$, where Γ is the toughness of the material and E is the Young's modulus. In soft failure, ℓ_{e} is larger than the fractocohesive length, the scale over which dissipative processes occur ℓ_{d}, defined as Γ/w^*, where w^* is the critical energy per unit volume for material failure.‡[9,10,14,15] Γ appears in both length scales and is typically estimated from experimental measurement by equating it with the critical energy release rate G at the onset of fracture. This approximation is only realistic for highly elastic materials whose stress concentration does not change during propagation,[12] an assumption we make throughout the manuscript in interpreting the experimentally-measured tearing energy. In such cases, $\Gamma \approx G \approx G_{\mathrm{t}}$ as well, which means that the observed or effective strain energy release rate does not include sizeable contributions from dissipative effects, *i.e.*, energetic contributions away from the crack tip that are not directly involved in surface creation.

This paper is organized as follows. We begin with the methods used to gather cutting, tearing, and uniaxial ultimate tensile property data followed by the results of these tests. Next, we use finite element analysis to verify that soft, ductile failure characterizes cutting-induced fracture, just as in tearing for these materials. The similarity of these failure modes justifies the search for a dimensionless cutting–tearing equivalency parameter, which we obtain *via* scaling analysis. Next, we closely describe the radius-dependence of cutting energy. First, Lake–Thomas theory is modified to describe the plateau observed in the cutting energy for sufficiently small blade radii. The modification, consisting of a larger-than-molecular-plane damage zone, is implemented as new failure criteria in finite elements. These criteria correctly predict the increase in apparent cutting energy when using blunted blades. Finally, we

---

‡ Hypothetically, w^* is quantifiable by determining the area under the force–displacement curve up to catastrophic failure and dividing by the sample volume, assuming a flaw-free sample.

discuss additional questions related to microstructural contributions to failure response raised by tests on bimodal PDMS formulations.

2 Materials and methods

2.1 Materials

We fabricate nine elastomer formulations: five commercially available polydimethylsiloxane (PDMS)-based elastomers and their variations, and five synthesized, end-linked networks having either a unimodal or bimodal chain-length distribution.

Sylgard 184. Two silica-nanoparticle-filled PDMS composites (Sylgard 184, Dow Corning) having different cross-link densities are prepared by controlling the crosslink density. A pre-polymer base to the curing agent ratio of 10 : 1 is used for both materials, (Syl-10 : 1 and Syl-d10 : 1), but the latter dilutes the network with 30 wt% linear non-reactive PDMS chains (350 cSt, Gelest, Inc.). Details of fabrication are documented in previous work.[4]

Solaris. Two Solaris elastomers (Smooth-On, Inc.) with differing cross-link density are fabricated by mixing part A and part B pre-polymer chains as received in 1 : 1 (Sol-1 : 1) and 4 : 1 (Sol-4 : 1) ratios (w : w), followed by degassing (∼20 min), molding, and curing at 70 °C for 1.5 h.

Unimodal. An end-linked unimodal PDMS network (UPDMS) combines vinyl-terminated PDMS chains (17 200 g mol^{-1}, Gelest, Inc., DMS-V25R) and a silane cross-linker (tetrakis(dimethylsiloxy) silane, Gelest, Inc., SIT7278.0) in a stoichiometric ratio of 1 : 1.4 (Si-vinyl groups to Si–H groups) using a centrifugal mixer (Speed-Mixer™) at 2000 rpm for 30 s. Platinum-based catalyst (platinum–divinyltetramethyldisiloxane complex in xylene, Gelest, Inc., SIP6831.2) diluted in toluene (1 : 100, w : w) is added at 0.5 ppm of platinum (by weight) into the mixture before mixing again at 1500 rpm for 30 s. The final mixture is degassed for 1 min if necessary and cast into a mold. The samples cure in approximately 2–3 h, then set overnight to remove residual toluene.

Bimodal. The four end-linked bimodal PDMS networks are fabricated following the formulations tabulated below. They are labeled according to the corresponding molar concentration of short chains (m_s): the silane cross-linker (Gelest, Inc., SIT7278.0) is added into and mixed with the vinyl-terminated PDMS long chains (Gelest, Inc.) and short chains (Gelest, Inc., DMS-V03) in a stoichiometric ratio of 1 : 1.2 (Si-vinyl groups to Si–H groups) in one pot using the centrifugal mixer at 2000 rpm for 1 min. Toluene-diluted platinum catalyst (1 : 100, w : w) is then added at 1 ppm of platinum (by weight) followed by mixing at 1500 rpm for 30 s and degassing for 1 min if needed. Samples are then cast into a mold and cure overnight after a working time of approximately 12 h.

2.2 Mechanical characterization

Y-shaped cutting. The cutting fracture responses of the selected elastomers are characterized using a Y-shaped geometry detailed previously.[4] Fig. 2b illustrates Y-shaped cutting in which two preloaded sample 'legs' are separated by a fixed angle, introducing a crack-opening, tearing component while minimizing the contact friction.[1,4] An orthogonally-mounted razorblade cuts the sample at a constant, controlled speed (10 ± 0.1 mm min^{-1}) while the required cutting force is measured by a load cell (M7-05, Mark-10™, range: ±2.5 N, resolution: 5×10^{-4} N). Two key improvements to the test geometry are: (1) the number of low-friction pulleys is increased to four (Fig. S1, ESI†). The new configuration of stringing enables a more stable cutting phase, a wider adjustable range for the leg angle, and a longer maximum cutting distance; (2) the applied average pre-stretch is now determined at a higher accuracy ($\bar{\lambda} = 1.04 \pm 0.01$ for all materials tested, unless otherwise stated) using a video extensometer. Technical information and nomenclature for both commercially-available and manually-blunted razorblades are listed in ESI,† including tip radii measured *via* scanning electron microscopy (SEM).

Pure-shear tearing test. Tearing energies are determined using a pure-shear, single-notched tearing test. The detailed testing procedures are documented elsewhere.[4,16] In this manuscript, we adopt a rectangular sample geometry (2 mm × 60 mm × 10 mm, $t \times w \times h$) with a ∼10 mm pre-cut length. A strain rate ∼0.002 s^{-1} ensures quasi-static loading.

Constitutive characterization. Uniaxial tension tests are performed using 'dogbone'-shaped samples following ASTM test standards for elastomer tension (ASTM D412-16, die type C). The samples are molded in a milled aluminum mold with polished surfaces to reduce superficial defects. Each sample is stretched quasi-statically (strain rate ≈0.02 s^{-1}) to the point of rupture. A load cell (M7-10, Mark-10™, range: ±50 N, resolution: 0.01 N) measures force while stretch is determined *via* a video extensometer and fiducial markers (Fig. 2b).

3 Results

In Y-shaped cutting, the energy required to produce a steady-state cutting response derives from the combination of an applied cutting contribution C primarily due to the force on the blade f_{cut} and a tearing contribution T due to the combination of a finite angle θ between the legs and the applied pre-load f_{pre} that prevents the sample from buckling. For a sample of thickness t, the applied strain energy release rate is[4]

$$G_{\text{cut}} = \underbrace{\frac{2f_{\text{pre}}\bar{\lambda}}{t}(1-\cos\theta)}_{T} + \underbrace{\frac{f_{\text{cut}}\bar{\lambda}}{t}}_{C}, \quad (1)$$

where $\bar{\lambda}$ is the average pre-stretch in the sample legs. In the limit of very low T, G_{cut} reaches a limit termed pure cutting.[1] In this limit, $T + C$ no longer depends on T (θ, $\bar{\lambda}$, or f_{pre}); further decrease in T is exactly balanced by an increase in the measured C. This suggests that an excess tearing contribution is no longer being applied and that only the minimum energy required to propagate a crack is being input. Unfortunately, the leg angle and applied pre-load to reach this limit is practically challenging as frictional effects can begin to play a role at low θ for very soft solids.[4] In this work, we use $\theta = 32° \pm 1°$ to approach pure cutting while avoiding frictional effects for all materials tested. (See ESI† for experimental T and C values.) Previously, we found $\theta \approx 15°$ to be the pure

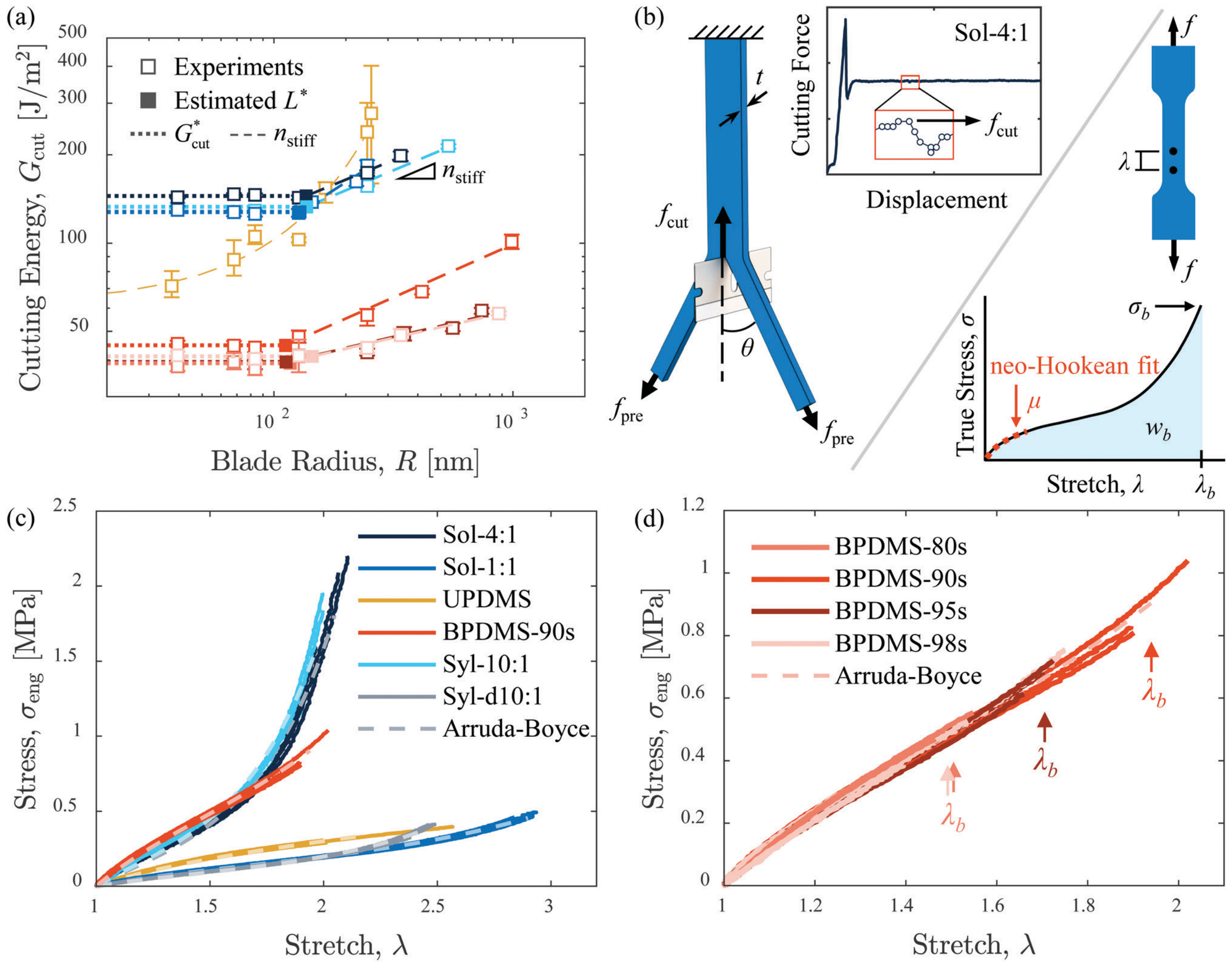

Fig. 2 Y-shaped cutting and material constitutive responses (a) G_{cut} *versus* blade radius R obtained *via* Y-shaped cutting (open symbols, $\theta = 32° \pm 1°$, $\bar{\lambda} = 1.04 \pm 0.01$). All materials except UPDMS exhibit a plateau at low blade radii (dotted lines, G^*_{cut}) that intersects with a power-law fit (dashed lines) having exponent n_{stiff} at larger blade radii. The intersection of these regimes occurs at length scale L^* (closed symbols). UPDMS is fit with the expression $\log_{10}[a + 10^{b(R-c)}]$ where a, b, and c are fit constants and we take $G^*_{cut} = a$. Colors match the legends in (c) and (d). Error bars are the maximum and minimum values of three or more samples at each R. (b) Left: A schematic of the Y-shaped cutting geometry. f_{pre} is applied on each of the sample legs to maintain a constant leg angle, θ. G_{cut} is determined from the maximum f_{cut} measured during steady-state cutting as shown by the subplot of typical data (Sol-4 : 1). Right: A dog-bone sample with fiducial markers to measure the stretch is used for uniaxial tensile tests to failure. The shear modulus is determined from a neo-Hookean fit to the stress–stretch curve (fit range: λ = 1–1.1). Ultimate properties w_b, σ_b, and λ_b are illustrated schematically. (c) Engineering uniaxial tension responses for all elastomers (solid lines). Each Arruda–Boyce fit shown (lighter dashed lines) is averaged between three samples (d) constitutive responses of four BPDMS samples exhibit identical elastic responses but different λ_b.

cutting limit for Syl-10 : 1.[4] However, G_{cut} for the larger angle used here is only 1.4 times the pure cutting value. Even for leg angles up to 48°, G_{cut} is only twice the pure cutting value.[4] Thus, we believe that the measured cutting energy we report here, though not exactly the pure cutting value for all materials, likely differs from pure cutting by much less than an order of magnitude. Such a difference will have little effect on the discussion and interpretation to follow.

We characterize elastomer samples using the Y-shaped cutting technique at varying blade radius and compare the response to standard failure tests: pure shear tearing and uniaxial tension to failure. In the cutting response, two cutting energy regimes exist for a broad range of silicone elastomers as shown in Fig. 2a, a plateau at low blade radii and a material non-linearity governed response at larger blade radii. The materials include a unimodal network UPDMS (in which the chains between crosslinks are nominally identical), bimodal networks BPDMS (in which two chain lengths are used), and the multimodal commercial networks Sylgard 184 and Solaris, with and without silica filler, respectively. Previously, we observed that outside of the plateau, the sensitivity of the cutting energy to an incremental increase in blade radius correlated with the large-strain nonlinear response of the material – a material with a stronger strain-stiffening effect exhibits less sensitivity for the same increment of the crack tip radius.[4] In the discussion to follow, we concretize this observation by correlating the radius sensitivity to the material's deformability in Section 4.3.

At a sub-micron characteristic transition length scale, the cutting energy reaches an observable plateau ($L^* \lesssim 100$ nm) for all of the silicone formulations we tested with the notable exception of the unimodal formulation UPDMS (Fig. 2a). In this latter case, it appears that the data trend toward a plateau, but that the transition likely occurs at a blade radius lower than experimentally achievable. Presumably, the onset of this transition L^* is smaller than the experimentally available blade radii (<37 nm).§ We determine L^* for all other materials using a two-sample Kolmogorov–Smirnov test[17] for data at differing blade radii and then refine the estimate using the intersection of a power law fit of the radius-sensitive region (exponent n_{stiff}) with the average value of the all the points that lie within the plateau. We call this minimum required energy the threshold cutting energy G^*_{cut}. L^* is marked by a closed symbol in Fig. 2a.

3.1 Ultimate properties from uniaxial testing

Ultimate properties are functions of both the constitutive response of a material and its failure onset. We measure these properties for each silicone formulation using quasi-static uniaxial tensile tests performed on dogbone samples made in smoothed molds (to minimize defects). The test geometry, definition of the ultimate properties extracted, and stress–stretch results are given in Fig. 2b–d. From their responses, we categorize the materials into three types:¶

- High modulus elastomers with strong strain-stiffening effects, *e.g.*, Syl-10 : 1 and Sol-4 : 1;
- Lower modulus elastomers with weaker or vanishing strain-stiffening effect approaching a more neo-Hookean response, *e.g.*, Sol-1 : 1, Syl-d10 : 1, and UPDMS;
- Elastomers whose overall behavior approaches linear, *e.g.*, all BPDMS's.

Their constitutive response is captured by the approximated incompressible Arruda–Boyce model[18,19] (ESI†). Ultimate tensile failure is described by maximum strain energy density w_{b}, stretch at break λ_{b}, and stress at break σ_{b}. As Fig. 2b illustrates, w_{b} is obtained from the area under the true stress *versus* stretch curve. λ_{b} is the maximum value of the recorded stretch. σ_{b} is the true stress at break, $\sigma_{\mathrm{eng}}\lambda_{\mathrm{b}}$. The shear modulus μ is determined for all materials using the low stretch ($1 \leq \lambda \leq 1.1$) portion of the curve. All data are provided in Table 2.

3.2 The stress concentration in cutting: determining length scales

Upon first glance, it is clear that the stress field for a crack tip propagating in cutting differs from that during tearing. The blade contact imposes a crack tip geometry,[4,20] which suppresses the crack blunting typically observed in elastomer failure while also introducing a compressive stress not found in tearing. Less obvious, however, is the relationship between the length scales thought to govern fracture. The relative size of these length scales are associated with the type of failure that occurs; we are primarily interested in the soft ductile behavior characterizing elastomers under far field tearing. A larger nonlinear elastic zone than dissipation zone, $\ell_{\mathrm{e}} \gg \ell_{\mathrm{d}}$,[9] defines this regime, with a crack size c on the same order as or smaller than the dissipation zone size, $c \lesssim \ell_{\mathrm{d}}$. The previously used scaling relations for these length scales $\ell_{\mathrm{d}} \sim \Gamma/w^*$ and $\ell_{\mathrm{e}} \sim \Gamma/\mu$,[8,9] are derived for asymptotic stress fields in far-field tearing and not for cutting, and therefore cannot be used directly. To determine whether the soft ductile regime still applies in cutting, analogous relations must first be determined for Y-shaped cutting.

Table 1 Chemical compositions of bimodal PDMS networks

Material	M_{l}[a] (g mol^{-1})	M_{s}[a] (g mol^{-1})	ω_{s}[b] (%)	m_{s}[b] (%)
BPDMS-80s	9400	500	18	81
BPDMS-90s	17 200	500	20	90
BPDMS-95s	28 000	500	25	95
BPDMS-98s	43 000	500	34	98

[a] Molecular weight of long (short) chains. [b] Weight percentage of short chains.

Analysis of the asymptotic stress field at crack tips in highly deformable solids has undergone significant recent development,[21–24] however in steady-state cutting or the related needle insertion, asymptotic fields are still calculated using finite element methods[5,25–28] or in some cases experimentally.[4,20,29] Like cracks under far-field loading, a stress concentration in cutting depends on a given cutting geometry and material response. For the Y-shaped geometry, we find that the stress concentration combines both the tearing component from the pre-load and the contact with the blade tip.

To compute the asymptotic stress field in cutting, we carried out finite element analysis (FEA) of cutting indentation. We model the Y-shaped experimental geometry in ABAQUS using a hyperelastic material (CPS8 quadrilateral plane stress elements) having fit coefficients matched to those obtained from uniaxial deformation (Arruda–Boyce). A pre-load equal to the experimental conditions is applied to the legs at an angle of 32° from the plane of symmetry. A rigid analytical surface with the geometry of a sharp razorblade indents with a force equal to that observed within the plateau cutting regime for each material simulated (Sol-4 : 1, Sol-1 : 1, and BPDMS-90s). (See ESI† for further technical detail.)

In the asymptotic limit near the crack tip, the stress field can be approximated by the superposition of fields from a compressive line load[31] on a half-plane and a V-shaped notch under tension.[30] For a compressive line load on a neo-Hookean half-plane (nonlinear Flamant problem), $\sigma_{11} \sim 1/r$ and $\sigma_{22} \sim -1/r$.[31] (This singularity changes little for a strain-stiffening, Arruda–Boyce half space as evidenced by FE simulations, see ESI.†) For a V-shaped notch in a hyperelastic solid, $\sigma_{11} \sim r^{(2\theta/\pi-1)} \sim 1/r^{0.64}$ ($\theta = 32 \pm 1$ degrees) and $\sigma_{22} \sim \sqrt{r}$.[30] In Fig. 3 we plot these singularities using dash and dashdot lines. The magnitudes of the crack opening stress, σ_{11}, and longitudinal stress, σ_{22}, are given along a line through the sample's plane of symmetry as a function of the distance from the crack tip, r as points which vary in color based on the constitutive model used. High saturation and low

---

§ For UPDMS, we take L^* as the smallest blade radius in Fig. 6.

¶ Fig. S3 in ESI† provides modulus normalized stress–stretch responses for comparison.

Table 2 Mechanical and failure characteristics of elastomers

Material	μ [MPa]	σ_b [MPa]	λ_b	w_b [MPa]	G_{tear} [J m^{-2}]	G^*_{cut} [J m^{-2}]	L^* [nm]	n_{stiff}	$\mathscr{E}_{CT}$
Sol-4 : 1	0.39 ± 0.03	4.01 ± 0.78	2.05 ± 0.07	1.08 ± 0.22	182.7 ± 23.9	144.7 ± 2.4	136.3	0.34 ± 0.06	0.127 ± 0.005
Sol-1 : 1	0.13 ± 0.02	1.37 ± 0.07	2.90 ± 0.05	0.86 ± 0.04	50.8 ± 9.6	127.7 ± 3.3	128.4	0.53 ± 0.11	0.316 ± 0.028
Syl-10 : 1	0.37 ± 0.05	3.33 ± 0.78	1.97 ± 0.04	0.90 ± 0.17	165.9 ± 9.0	132.9 ± 3.4	137.1	0.34 ± 0.04	0.141 ± 0.019
Syl-d10 : 1	0.09 ± 0.01	0.93 ± 0.14	2.44 ± 0.06	0.43 ± 0.06	43.0 ± 2.7	77.5 ± 2.9	161.1	—	0.261 ± 0.025
UPDMS	0.17 ± 0.02	0.74 ± 0.24	2.19 ± 0.32	0.44 ± 0.26	29.7 ± 3.1	61.3 ± 6.0	$\lesssim$37.4	0.83 ± 0.23	0.384 ± 0.086
BPDMS-80s	0.44 ± 0.01	0.76 ± 0.09	1.50 ± 0.05	0.18 ± 0.04	33.2 ± 7.2	39.0 ± 3.3	117.0	—	0.163 ± 0.013
BPDMS-90s	0.48 ± 0.08	1.74 ± 0.31	1.94 ± 0.07	0.70 ± 0.16	28.2 ± 5.4	44.8 ± 1.3	111.9	0.36 ± 0.04	0.243 ± 0.008
BPDMS-95s	0.47 ± 0.07	1.14 ± 0.11	1.70 ± 0.03	0.35 ± 0.05	37.2 ± 4.0	39.4 ± 1.2	112.4	0.19 ± 0.04	0.190 ± 0.001
BPDMS-98s	0.48 ± 0.08	0.75 ± 0.35	1.49 ± 0.17	0.19 ± 0.14	39.0 ± 3.8	41.2 ± 1.1	144.7	0.18 ± 0.03	0.145 ± 0.031

Error corresponds to the standard deviation of three or more samples.

saturation colors correspond to tensile (+) and compressive (−) stresses, respectively. In the direction of load application by the blade, σ_{22}, the superposition of the two analytical fields yields $\sigma_{22} \sim -1/r$ when taking the dominant asymptote as $r \to 0$. As anticipated, σ_{22} is compressive rather than tensile as in far-field tearing. In the crack opening direction, the $\sigma_{11} \sim 1/r^{0.64}$ asymptote arising from the V-shaped notch dominates, with $\sigma_{11} \sim 1/r$ contributing to a small upturn in the slope nearest the crack tip. On average the power-law dependencies in the region $r \sim 0.1$–1 mm from the crack tip for all three materials equal $r^{-0.67\pm0.04}$, certainly weaker than the $1/r$ dependence for far-field tearing. A similar, sub-inverse power-law dependence has been reported for blade penetration into a hyperelastic substrate.[5] For comparison, the crack-opening (σ_{11}) singularity for an initially parallel crack in a nonlinear, highly deformable solid subjected to far-field loading is $1/r$,[9,21,22] indicated by the lower gray dash-dotted line in Fig. 3a.

The discrepancy between the stress concentration in Y-shaped cutting and that observed in far-field tearing changes the length

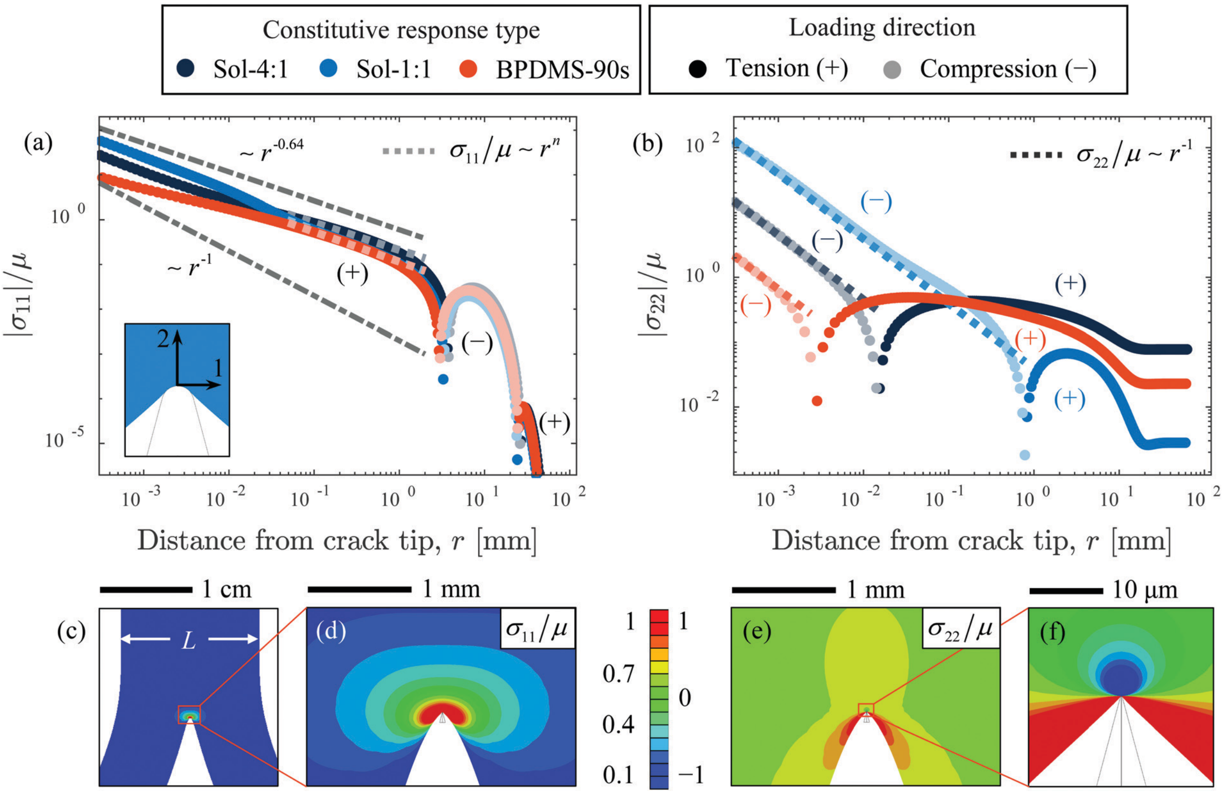

Fig. 3 Asymptotic crack fields from simulated stress responses in a Y-shaped loading geometry. Loading conditions correspond to those observed within the threshold regime. High color saturation and low color saturation points correspond to tensile (+) and compressive (−) stresses, respectively. (a) Normalized crack-opening stresses (σ_{11}) along a line through the sample center (*i.e.*, the crack path). Power-law fits of the near crack-tip regime ($\sigma_{11}/\mu \sim r^n$, fit range: r = 0.1–1 mm) are shown with light-colored dotted lines. For comparison, a r^{-1} singularity (lower gray dash-dotted line) corresponding to an initially parallel far-field crack and a $r^{-0.64}$ singularity (upper gray dash-dotted line) corresponding to the theoretical hyperelastic V-notch response[30] are shown. (b) Normalized longitudinal stresses along the crack path. The near crack-tip asymptotic behavior follows a r^{-1} singularity (saturated dotted lines) corresponding to the nonlinear Flamant response[31] for all materials. (c) Contour plots of σ_{11}/μ in a Sol-4 : 1 like material captured at the sample length scale and (d) $r \sim 1$ mm, respectively. (e) Contour plots of σ_{22}/μ in a Sol-4 : 1 like material illustrate tension far from the crack tip ($r \sim 1$ mm) and compression at (f) $r \sim 10$ mm.

scales ℓ_e and ℓ_d. Here, we numerically approximate both length scales for Y-shaped cutting in a subset of our materials using our finite element results in Fig. 4. We take as the threshold of the onset of strong nonlinearity, the stretch λ_e at which the uniaxial stress becomes comparable to the Young's modulus E for each material ($\lambda_e \sim 2$–3 in all cases). In the crack opening direction (Fig. 4a), this threshold $\lambda_{11} = \lambda_e$ corresponds to a given distance $r = \ell_e$ from the crack tip. The resultant ℓ_e values are listed in Table 3. The specifics of these numerical estimates are unimportant, however the ℓ_e obtained in this way ($\approx$2–7 μm) are at least an order of magnitude smaller than those estimated from the elastocohesive length of far-field tearing, G_{tear}/E ($\ell_{\text{e,tear}} \approx 20$–154 μm) (Table 3). Similarly, the dissipation length scale ℓ_d estimated for far-field tearing using the strain energy density at break G_{tear}/w_b[9] yields a value of $\ell_{\text{d,tear}} \sim 40$–169 μm. We numerically approximate the corresponding dissipation length scale for Y-shaped cutting by determining the distance from the crack tip r at which the strain energy density at break is reached, $w = w_b$ (Fig. 4b). We find that $\ell_d \approx 1$–4 μm (Table 3), again at least an order of magnitude less than that encountered in tearing. Both of these dissipation values are upper bounds since w_b measured experimentally is likely reduced from the threshold energy density for material failure w^* due to the unavoidable presence of flaws in the sample. Taking the blade radius R as the length scale defining crack size c, it follows that despite the constraints on crack tip deformation provided by the blade (resulting in less blunting), silicone elastomers still behave as soft ductile materials under Y-shaped cutting since $\ell_e > \ell_d$, and $c \lesssim \ell_d$. The most significant difference between the two failure geometries is the greatly reduced magnitude of both ℓ_e and ℓ_d during cutting, which suggests that the Y-shaped geometry satisfies small-scale yield conditions even when performed on highly deformable materials.

Table 3 Fracture relevant length scales for selected elastomers (unit: μm)

Material	ℓ_e	$\ell_{\text{e,tear}}$	ℓ_d	$\ell_{\text{d,tear}}$
Sol-4 : 1	3.0	153.8	1.1	168.7
Sol-1 : 1	6.9	131.5	4.2	58.8
BPDMS-90s	1.7	19.5	1.0	40.3

Outside of the asymptotic region near the crack tip, the stress-state in the sample along the axes of symmetry behaves as anticipated, with a few small anomalies attributed to the plane stress constraint of the simulation. As their presence does not affect the deformation and failure length scales near the crack tip, their discussion is left to the ESI.†

4 Discussion

In this section we discuss the two primary characteristics governing macroscopic failure onset in highly elastic, elastomeric solids: (1) deformability and (2) local, threshold rupture criteria. The former is embodied by a material's constitutive response and the latter, ideally, by its rupture in the absence of flaws. We validate this picture of soft fracture through the identification of a dimensionless group that induces proportionality between cutting and tearing. We also identify these failure characteristics in the radius dependent response of G_{cut} presented in Fig. 2. At small radii, we interpret the plateau as the minimum energy required to activate a threshold damage zone with characteristic size $\ell^* \sim L^*$. Evidence for this assertion is provided by agreement between this minimum energy and the general framework originally postulated by Lake & Thomas.[32] For larger radii, we implement the idea of a critical minimum damage zone in finite element simulation, which

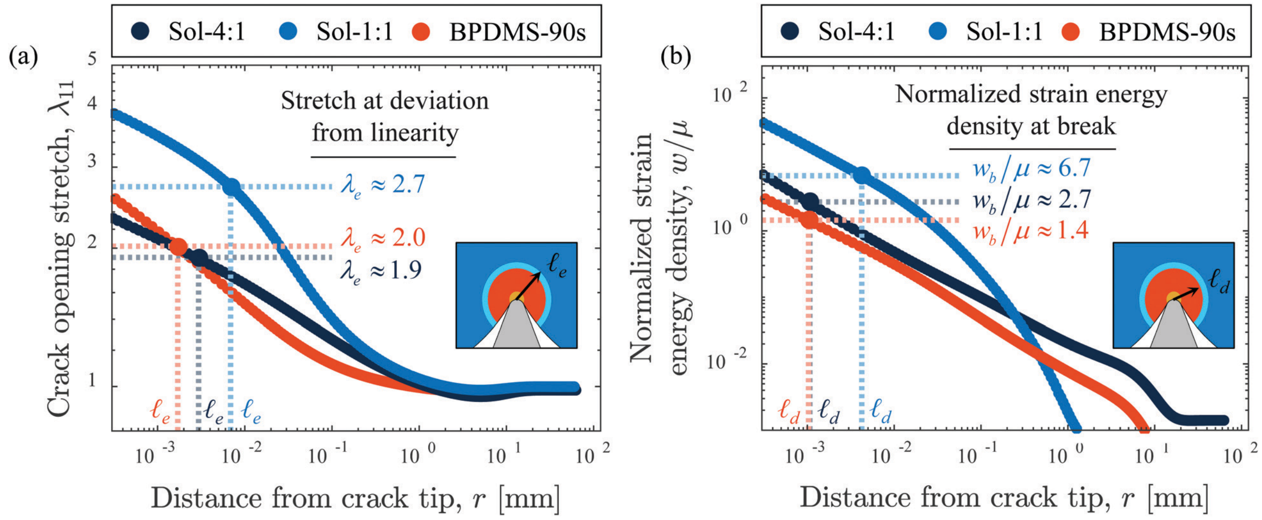

Fig. 4 Determining fracture length scales from simulated stretch and strain energy density in a Y-shaped cutting geometry. (a) The crack-opening stretch λ_{11} along the crack path. The intersection of λ_{11} with the experimentally-determined onset of nonlinear elasticity λ_e (horizontal dotted lines) determines the distance from the crack tip corresponding to the onset of nonlinear elasticity ℓ_e (vertical dotted lines). (b) The shear modulus-normalized strain energy density w/μ along the crack path. Each curve is intersected by experimentally-observed strain energy density at break w_b/μ (horizontal dotted lines) to determine the dissipation length scale ℓ_d (vertical dotted). Insets: Illustrations of the nonlinear elastic zone (teal) and the dissipation zone (red) near the crack tip.

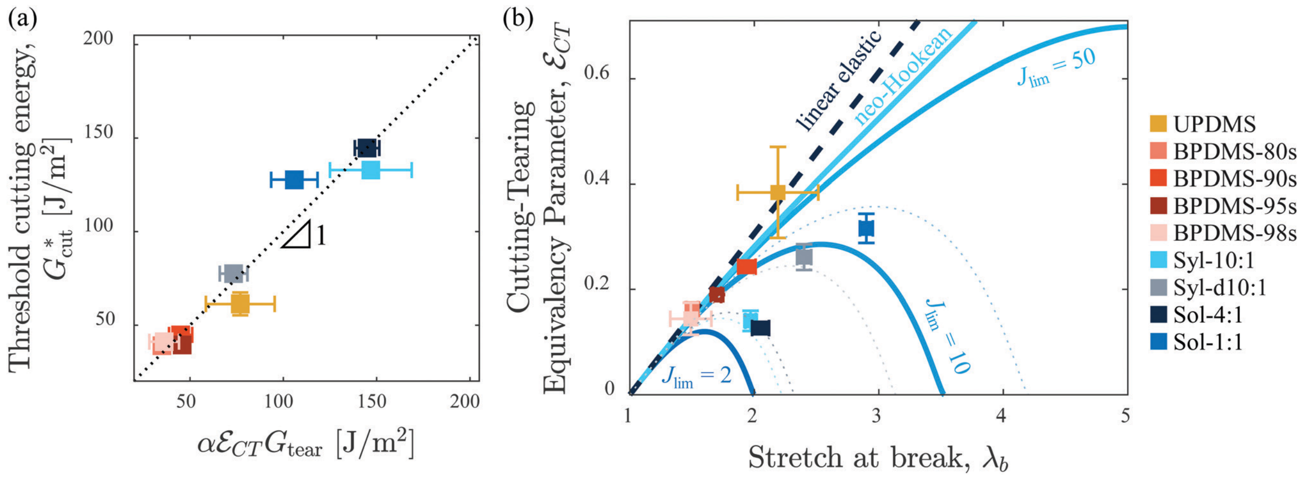

Fig. 5 Mapping cutting and tearing using the equivalency parameter, $\mathcal{E}_{\mathrm{CT}}$. (a) Cutting energy is linearly proportional to the product of tearing energy and $\mathcal{E}_{\mathrm{CT}}$ for the hyperelastic silicones tested. The fit constant $\alpha = 7.2$ allows the data to be plot on a zero intercept line of slope one (black dotted). (b) A plot of $\mathcal{E}_{\mathrm{CT}}$ *versus* the stretch at break λ_{b} for a linear elastic material (dark dashed line), neo-Hookean (teal line), and a Gent material with decreasing limiting stretch (decreasing J_{lim} corresponds to increasing color saturation). Experimentally-determined $\mathcal{E}_{\mathrm{CT}}$ and λ_{b} values are provided for comparison. For Sol-1 : 1, Sol-4 : 1, Syl-10 : 1, and Syl-d10 : 1, a corresponding Gent behavior line (dotted line) is added using J_{lim} determined from a fit to the response in Fig. 2a. Error bars are determined from the standard deviation of three or more samples. The legend at the right applies to both plots.

leads to an increase in cutting energy with increasing radius that is quantitatively consistent with experimental observation. Qualitatively, more deformable, neo-Hookean-like materials require a larger cutting energy increment per given increase in blade radius. Together this combination of observation and modeling point provide a description of the interplay of factors governing failure in elastic, highly deformable polymer networks.

4.1 Mapping cutting and tearing

Unlike tearing energy which can obtained from a variety of sample geometries,[33] the characteristic energy required to cut a sample must be carefully chosen. The Y-shaped geometry minimizes frictional effects and avoids failure initiation through steady-state operation. Additionally, the cutting energy plateau in Fig. 2a suggests that for sufficiently small radius, the stress increase from sharper tools occurs within a volume that is too small to include the microstructural features necessary for fracture.[34] Thus within this plateau, the cutting energy G^*_{cut} represents a characteristic threshold cutting energy. For this reason, we compare the threshold cutting energy value with the tearing energy taken from pure shear tests G_{tear}. This comparison finds that in some cases, threshold cutting energy is less than the tearing energy (below the dashed line in Fig. 1a) and in others, it is greater (above the dashed line in Fig. 1a). A closer look reveals that materials exhibiting higher cutting energy exhibit a tendency toward a neo-Hookean response (Fig. 2c). Those exhibiting higher tearing energy appear to be more highly non-linear and strain-stiffening. The most brittle materials, whose overall behavior approaches linear, lie closest to a one-to-one correspondence between cutting and tearing energy. In quantitatively converting between the cutting and tearing energies for all three classes of material response we must account for both intrinsic failure onset and constitutive response.

In addition to cutting and tearing, ultimate strength tests of un-notched samples provide an additional measure of a material's failure response. They have the added benefit of simultaneously characterizing information about a material's finite deformability. The quantities w_{b}, σ_{b}, and λ_{b} are the toughness, stress at break, and stretch at break and their relative proportions to one another reflect a material's constitutive response while their magnitudes provide an indication of its intrinsic failure response (Fig. 2b–d). Using Rayleigh's method of dimensional analysis, we find that the introduction of a dimensionless pre-factor that is a function of these ultimate properties and the shear modulus μ quantitatively and proportionally maps G^*_{cut} and G_{tear} (Fig. 5a). This cutting–tearing equivalency parameter $\mathcal{E}_{\mathrm{CT}}$ is defined as

$$\mathcal{E}_{\mathrm{CT}} \equiv \sqrt{\frac{w_{\mathrm{b}}}{\mu}}\left(\frac{w_{\mathrm{b}}}{\sigma_{\mathrm{b}}(\lambda_{\mathrm{b}}-1)}\right)^2. \qquad (2)$$

The powers 1/2 and 2 corresponding to each of the two dimensionless terms along with a constant $\alpha = 7.2$ arise from numerical fitting‖ subject to a constraint of linear proportionality between G^*_{cut} and G_{tear}. Thus the relation

$$G^*_{\mathrm{cut}} = \alpha\mathcal{E}_{\mathrm{CT}}G_{\mathrm{tear}}, \qquad (3)$$

collapses on the line in Fig. 5a. This collapse is not possible for other arbitrary combinations of parameters we tested. For highly elastic silicones, eqn (3) enables estimation of the threshold cutting energy from experimental tearing energies and ultimate tensile properties or *vice versa*. It will be important to test the generality of this expression on more constitutive response types and failure behaviors.

‖ Similar scaling is observed from a generic fit of the form $G_{\mathrm{cut}} = \alpha w_{\mathrm{b}}^{n_1}\mu^{n_2}\sigma_{\mathrm{b}}^{n_3}(\lambda_{\mathrm{b}}-1)^{n_4}G_{\mathrm{tear}}^{n_5}$, where α and n_i are fit parameters. We note that this more general fit contains six fit parameters and we have fit only six major types of materials responses, given the similarity of the BPDMS materials.

The cutting–tearing equivalency parameter is determined heuristically, but can be better understood through its evaluation using several classic constitutive models. In the limit of a linear material response, $\mathscr{E}_{\mathrm{CT}}$ is proportional to the strain at break, $\varepsilon_{\mathrm{b}} = \lambda_{\mathrm{b}} - 1$. That is, for a linear material under uniaxial tension, $w_{\mathrm{b}}/\mu \approx \frac{3}{2}\varepsilon_{\mathrm{b}}{}^2 = \frac{3}{2}(\lambda_{\mathrm{b}} - 1)^2$ and $w_{\mathrm{b}}/(\sigma_{\mathrm{b}}\varepsilon_{\mathrm{b}}) = w_{\mathrm{b}}/(\sigma_{\mathrm{b}}(\lambda_{\mathrm{b}} - 1)) = 1/2$. Thus $\mathscr{E}_{\mathrm{CT}} = \sqrt{\frac{3}{32}}(\lambda_{\mathrm{b}} - 1)$ (Fig. 5b, dark blue dotted line). For a neo-Hookean solid, $\mathscr{E}_{\mathrm{CT}}$ differs little from the linear response (Fig. 5b, teal solid line), but becomes non-monotonic in λ_{b} in the case of a strain stiffening material as stretch approaches a limiting value (Fig. 5b, solid lines of increasing saturation). We employ a simple Gent model in Fig. 5b to capture the effect of a limiting stretch, which produces behavior similar to that of Arruda–Boyce. For this model, limiting stretch occurs when the first invariant of the left Cauchy–Green deformation tensor I_1 reaches a limiting value $J_{\mathrm{lim}} + 3$ as illustrated by the strain energy density function

$$W = -\frac{\mu J_{\mathrm{lim}}}{2}\ln\left(1 - \frac{I_1 - 3}{J_{\mathrm{lim}}}\right). \tag{4}$$

All three of these material responses are special cases in which w_{b} and σ_{b} are both proportional to μ, leaving $\mathscr{E}_{\mathrm{CT}}$ independent of the modulus. For context, the calculated $\mathscr{E}_{\mathrm{CT}}$ values for each of the materials tested here are provided in Fig. 5b and Table 2. Those that exhibit a finite J_{lim} according to a Gent fit of the uniaxial stress strain response in Fig. 2c, are accompanied by a light, dashed curve for that J_{lim} fit value.

We can also try to understand $\mathscr{E}_{\mathrm{CT}}$ from a comparison of the physical quantities that comprise the dimensionless ratios w_{b}/μ and $w_{\mathrm{b}}/[\sigma_{\mathrm{b}}(\lambda_{\mathrm{b}} - 1)]$ in it. These ratios are similar, but not identical to, previous dimensionless quantities found in the literature. For example, recently, the strength of soft elastic membranes was modeled using a w_{b}/μ-like threshold for hole growth.[35] w_{b}/μ also shares some similarity with Ashby's flexibility index σ_{b}/μ.[36] Essentially it is a ratio of energetic toughness to stiffness. The ratio $w_{\mathrm{b}}/[\sigma_{\mathrm{b}}(\lambda_{\mathrm{b}} - 1)]$ normalizes the stored elastic energy by the sum of the complementary strain energy** and the stored energy. Visually, it is the fraction of the rectangle defined by the stress and strain at break as swept out by the area under the actual stress–stretch response. To our knowledge these dimensionless groups have not previously been combined to describe the failure response of soft, deformable solids.

4.2 A minimum length scale for failure

Lake & Thomas described the failure threshold in polymer networks as being dictated by the energy released from the rupture of a single molecular plane of polymer chains.[32] This qualitative picture of the minimum energy for surface creation is beginning to be challenged. For instance, theories suggest it is associated with massive bond breakage[37] or that it should consider energetic contributions from a few network layers neighboring the failure plane.[38] These suggest that the chain rupture required for surface creation is not confined to a single molecular plane. Recent experimental visualization of covalent bond breakage *via* mechanophores finds that covalent bond scission occurs over a diffuse volume near the crack in addition to the newly created surface.[39] The diffuse damage region reduces to the limits of resolution of the optical technique, ∼3 μm, in the absence of viscosity. In our results, the transition to the cutting threshold response occurs at an even smaller length scale, blade radii around 100 nm, but still approximately an order of magnitude larger than an average mesh size in most cases.†† Several observations further support the idea that onset of this threshold arises from a localized failure response deriving from the microstructural characteristics of the polymer network:

- The length scale of onset L^* appears to be unaffected by the angle between the legs and is therefore a material response.[4]
- L^* is an order of magnitude smaller than both ℓ_{e} and ℓ_{d}, the nonlinearity and dissipation length scales estimated from bulk properties, respectively.
- L^* is not governed solely by the presence of silica filler particles (∼100 nm), since it is similar for multi-modal networks with and without filler (Sylgard 184 *versus* Solaris and Bimodal networks, respectively).

In support of the idea of a threshold damage volume for surface creation, a modified Lake–Thomas theory,[32] requiring failure of all chains within the threshold length scale as opposed to a single molecular plane, gives order-of-magnitude agreement with the experimentally-observed threshold cutting energy G^*_{cut} (Fig. 6). Without the L^*-sized damage zone, Lake–Thomas theory underestimates G^*_{cut} by an order of magnitude.

A critical element of the Lake–Thomas prediction is the magnitude of the bond energy released upon chain scission. Lake–Thomas theory predicts that the threshold energy for failure is given by the expression[32]

$$G_{\mathrm{LT}} = \sqrt{\frac{3}{8}}\nu_{\mathrm{x}}\langle r_0\rangle N_{\mathrm{x}} U \tag{5}$$

where $\langle r_0\rangle$ is the average distance between crosslinks that defines the single molecular plane for failure. ν_{x} is the bulk density of crosslinks and N_{x} is the average number of backbone bonds between crosslinks, each of which release a bond energy U when a network chain is broken. We determine ν_{x} and N_{x} from a network elasticity model[39,40] and the stress–stretch curve (see ESI†). The thickness of the molecular plane, which ranges from 5–15 nm, comes from the expression $\langle r_0\rangle = l_0\sqrt{C_\infty N_{\mathrm{x}}}$, where l_0 is the length of a backbone bond (0.165 nm for Si–O[41]), and $C_\infty \approx 6.4$ is the Flory characteristic ratio for PDMS chains[41] (see ESI† for $\langle r_0\rangle$ values).

Recently, it has been suggested that the value for U used by Lake & Thomas, the bond dissociation energy ($\approx 7.36 \times 10^{-19}$ J for Si–O bonds[41]), provides a significant overestimate of the

---

** The principle of minimum complementary energy is typically used for linear elastic materials.

†† Only the unimodal network approaches, though it does not reach, the theoretical mesh size.

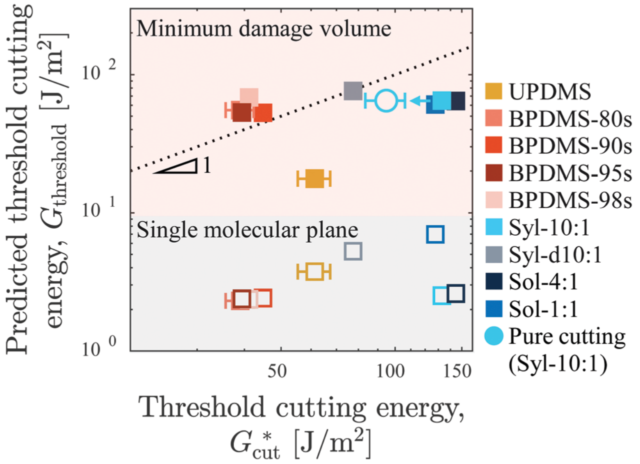

Fig. 6 Threshold failure energy $G_{\text{threshold}}$ predicted using a threshold damage volume (solid symbols, eqn (7)) and the traditional single molecular plane of Lake–Thomas theory (open symbols, eqn (5)). Predictions are compared to the experimentally observed threshold cutting energy G^*_{cut}; an exact match falls on the black dotted line of slope one defined by $G_{\text{threshold}} = G^*_{\text{cut}}$. To illustrate possible deviation of G^*_{cut} values from the pure cutting energy, a light blue arrow and circular symbol are provided for the pure cutting response of Syl-10 : 1. Error bars are the standard deviation of all samples lying within the dotted plateau in Fig. 2a.

energy released when the chain between cross-links breaks.[39,42] A more accurate estimation is obtained from the single strand stretch behaviors predicted by the modified freely-jointed chain model and the associated enthalpic distortion energy per bond, U_e[42]

$$U \approx U_e = \frac{1}{2}\frac{f_b^2}{f_s} l_0, \qquad (6)$$

where f_b is the breaking force of a main chain covalent bond and f_s is a characteristic stretching force. A typical breaking force for a Si–O bond is $f_b \approx 3.35$ nN[43,44] and the characteristic stretching force may be estimated as $f_s = k_{\text{Kuhn}} b$ where k_{Kuhn} is the stiffness of a Kuhn segment and b is the Kuhn length. We obtain values for k_{Kuhn} and b by fitting experimental force *versus* extension data for a single PDMS strand from the literature[45] using the modified freely-jointed chain model[42,43] to find that $k_{\text{Kuhn}} \approx 12.9$ N m^{-1} and $b \approx 1.47$ nm (see ESI†). As a result, $U_e \approx 4.89 \times 10^{-20}$ J, a factor of ∼15 less than the bond dissociation energy.‡‡ As a result, the threshold failure values predicted by the Lake–Thomas model fall an order of magnitude below the observed threshold cutting energy (Fig. 6, $G_{\text{threshold}} = G_{\text{LT}}$ within the gray region).

Motivated by the threshold in G_{cut}, we employ L^* to enlarge the damage zone beyond the molecular plane by replacing the molecular plane, $\langle r_0 \rangle$, with it. This simple modification,

$$G_{\text{LT,m}} = \sqrt{\frac{3}{8}}\nu_x L^* N_x U = \left(\frac{L^*}{\langle r_0 \rangle}\right) G_{\text{LT}} \qquad (7)$$

restores agreement between the concept of molecular scission proposed by Lake–Thomas and the threshold cutting energy in a highly elastic material as quantified by G^*_{cut}. Fig. 6 illustrates the shift in the predicted threshold $G_{\text{threshold}}$, where $G_{\text{threshold}} = G_{\text{LT,m}}$ within the light orange region. Agreement is indicated by proximity to a dotted line of slope one.

Though all materials we test are highly elastic, the modified theory best quantifies the response of the most brittle, least viscous of these (BPDMS and diluted Sylgard 10 : 1) as evidenced by their nearness to a line of slope one (Fig. 6). The approximation appears to slightly underestimate the threshold cutting energy for all other materials. However, it may also be that the measured G^*_{cut} is a slight over-estimation since no model materials or conditions are perfect. First, there can never be a complete absence of viscous or hysteretic effects. Thus, despite the very small region within which these effects may arise during cutting (small ℓ_e and ℓ_d), they certainly do occur to some extent and would lead to an increase in the force required to attain the minimum damage zone and thus the corresponding failure energy. Second, though we have made an effort to use a small angle θ between the legs, practical considerations have required a larger value than that associated with a pure cutting response[1] to maintain the consistency of test conditions for all materials. Thus, we may have an additional tearing energy component T (eqn (1)). A concrete example using Sylgard 184 10 : 1 illustrates this point. For this formulation, we previously observed a pure cutting energy of $\approx 95 \pm 10$ J m^{-2} ($\theta = 11$–$14°$),[4] a small decrease from the value we report here ≈ 133 J m^{-2} ($\theta = 32 \pm 1°$). An arrow toward the circular symbol in Fig. 6 indicates the deviation in the G^*_{cut}. Both of these rationale suggest that for some materials G^*_{cut} may be a small overestimate of the true threshold cutting response. However, they also provide promising avenues for future inquiry.

4.3 Achieving a minimum damage zone with increasing blade radius

Above the radius-independent cutting energy threshold, the energy required for steady-state cutting increases. We observe that the sensitivity of this increase to blade radius depends on the material being cut, with more stretchable samples requiring a higher cutting force for an incremental increase in blade radius (n_{stiff} in Fig. 2 and Table 2). To describe the mechanism behind these observations, we adopt the concept of a high deformation zone governing the localized damage necessary for surface creation.[7,9,12] We will show that when the threshold length scale L^* determines the size of this zone and the threshold cutting energy G^*_{cut} sets the magnitude of the strain energy density within the damage zone, we quantitatively recover the experimentally observed sensitivity of G_{cut} to R.

Using finite element simulation, we find that the size of the damage zone relative to the blade radius leads to two indentation force regimes, similar to the two G_{cut} regimes of experimental observation. The limits of the damage zone are determined numerically by setting a threshold value for the strain energy density; any elements meeting or exceeding this threshold criteria

---

‡‡ This order of magnitude agrees with an estimation from the force–stretch response of a single wormlike chain having average persistence length $p \approx 0.31$ nm which yields 1.7×10^{-20} J (see ESI†).

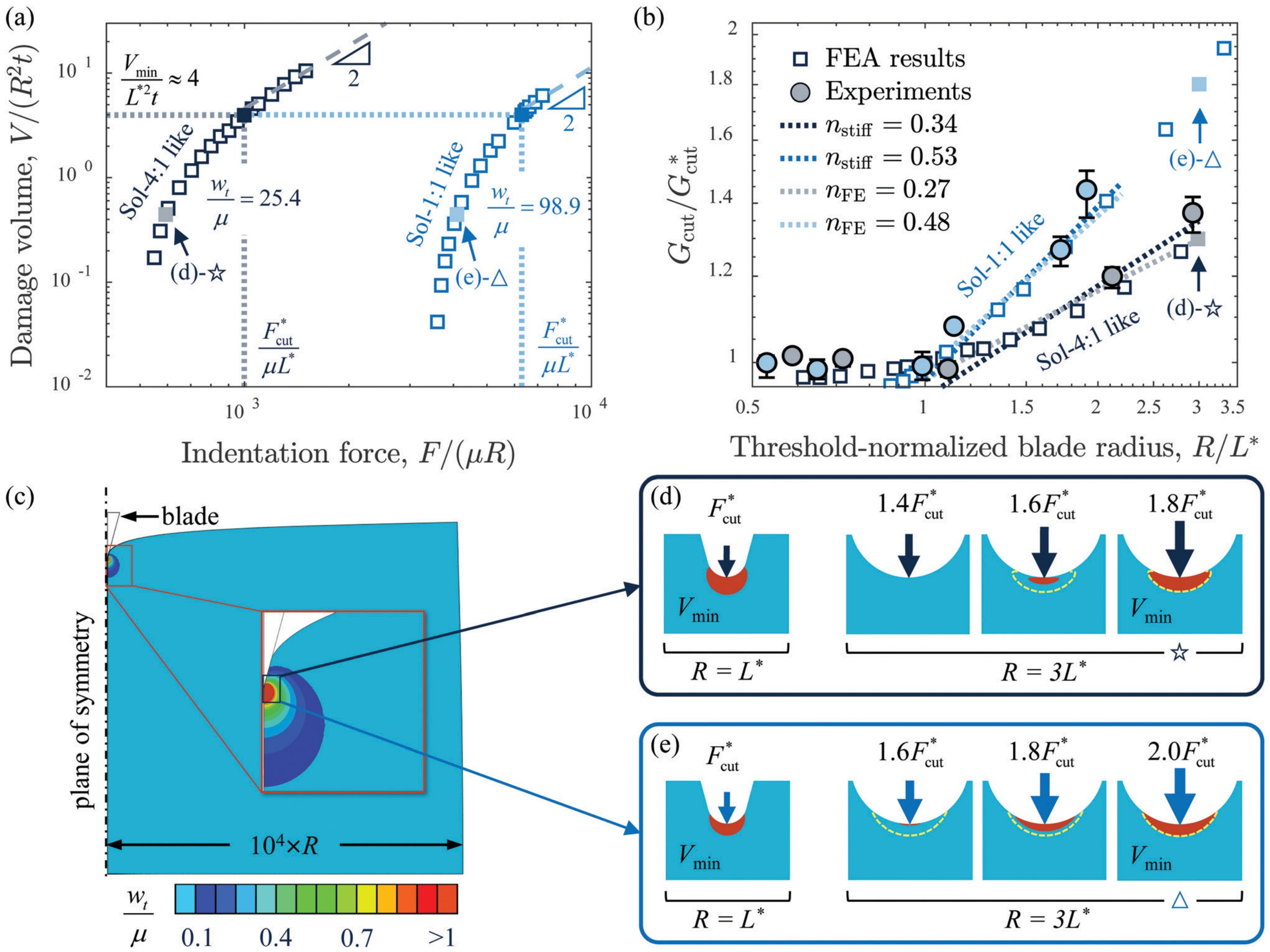

Fig. 7 Using a minimum damage volume to predict the radius-dependence of G_{cut}. (a) The relationship between normalized damage volume $V/(R^2t)$ and normalized force per unit thickness $F/(\mu R)$ as obtained from FE simulation of a blade indenting a hyperelastic Arruda–Boyce half-plane. The threshold strain energy density w_t/μ used to determine the volume was selected such that at $V_{min}/(L^{*2}t) \approx 4$ the normalized force per unit thickness matches that observed experimentally (filled solid squares and dotted lines) for either a Sol-4 : 1 like material (dark blue) or a neo-Hookean Sol-1 : 1 like material (light blue). Light-colored solid squares mark $V_{min}/(L^{*2}t) \approx 4/9$ and the $F/(\mu R)$ that correspond to $R = 3L^*$ for each material as shown in parts (d) and (e). (b) The force predictions in (a) are converted to normalized cutting energy G_{cut}/G^*_{cut} according to eqn (1) to illustrate the radius dependence of the cutting energy. Power law fits of the cutting energy increase predicted by FE (n_{FE}, light dotted lines) compare favorably with those determined experimentally (n_{stiff}, darker dotted lines). Experimental data from Fig. 2 is shown for comparison (circles). Light-colored solid squares again correspond to $R = 3L^*$ as shown in parts (d) and (e). (c) FE illustration of a blade indenting a half-plane. The size of the FE half-plane is approximately four orders of magnitude larger than the blade radius. A dash-dotted line indicates the plane of symmetry. Inset: A close-up of the near-tip strain energy density field, normalized by the shear modulus. (d) and (e) FE visualization of the evolution of the threshold damage volume as a function of radius R and cutting force: (d) Sol-4 : 1 like and (e) Sol-1 : 1 like materials. In both examples, the left image corresponds to the onset of the threshold cutting regime $R = L^*$, which requires force F_{cut} and defines V_{min}. The radius is tripled in the right images, requiring a force larger than the threshold value for the damage zone (red region) to attain V_{min}. Correspondence with parts (a) and (b) are indicated by star and triangle symbols for the Sol4 : 1 like and Sol-1 : 1 like responses, respectively.

are accounted to be in the damage volume V. Fig. 7a illustrates the normalized volume $V/(R^2t)$ of the damage zone and its relation to the applied normalized force per unit thickness $F/(\mu R)$ for simulation of a wedge with tip radius R indenting an elastic half-plane of thickness t. Two sets of constitutive parameters, matching Sol-1 : 1 (light blue) and Sol-4 : 1 (dark blue) are simulated. Sol-1 : 1 exhibits a more neo-Hookean response, while Sol-4 : 1 exhibits strain stiffening. When the size of the damage zone is large, $V/(R^2t) \gg 1$, the logarithmic slope approaches two and therefore $V/(R^2t) \sim \left(\frac{F}{\mu R}\right)^2$ making the required force to reach V independent of R, or $F \sim \sqrt{V\mu^2/t}$. When the damage zone is small relative to the blade radius, $V/(R^2t) < 1$ the constitutive response of the solid governs the dependence as evidenced by the difference in slope for different materials on a log–log scale. The Sol-1 : 1 like material shows a higher sensitivity of the required force to the radius in comparison to the Sol-4 : 1 like material, qualitatively matching the experimentally-observed trend that the power law dependence of G_{cut} on radius n_{stiff} for Sol-1 : 1 is greater than Sol-4 : 1. In effect, the more neo-Hookean, Sol-1 : 1 like material deforms more easily around the applied blade, so achieving the threshold damage zone size requires a larger force.

A critical component of this simulation is the choice of the threshold value for the strain energy density that determines the damage zone volume. We call this threshold w_t. The two indentation force regimes are only visible when the normalized critical strain energy density w_t/μ that sets the outer boundary of V corresponds to large deformation, $\lambda \gtrsim 2$. Thus within V, the strain energy density exceeds w_t/μ and the material is highly deformed $\lambda \gg 2$. The choice of w_t also establishes the position of the curve along the x-axis. The curve translates positive or negative when w_t/μ is increased or decreased, respectively (see ESI†).

To develop a quantitative comparison between the FE response and the experimental data we begin with two assumptions: (1) the minimum damage zone size is roughly determined by the blade diameter at the onset of the cutting threshold, $2L^\star$, so that $V_{\min} = (2L^\star)^2 t$ and (2) at the onset of the cutting threshold, the normalized force per unit thickness matches that measured in the cutting plateau. The former sets the reference point for the y-axis in Fig. 7a at $V/(R^2t) = V_{\min}/(L^{\star 2}t) = 4$. The experimentally-observed thickness-normalized cutting force value within the plateau regime is given by $F^*_{\mathrm{cut}} = f^*_{\mathrm{cut}}/t$. We determine that thresholds of $w_t/\mu = 25.4$ and $w_t/\mu = 98.9$ for Sol-4 : 1 like and Sol-1 : 1 like materials, respectively, satisfy both requirements as indicated by the dotted lines in Fig. 7a.

Next, we re-cast these indentation force results in terms of cutting energy. For a constant applied tearing contribution, eqn (1) yields

$$G_{\mathrm{cut}} = T + \frac{f_{\mathrm{cut}}\bar{\lambda}}{t} \approx T + F_{\mathrm{cut}} \tag{8}$$

where we have simplified the expression by noting that the applied pre-stretch is close to 1, $\bar{\lambda} \approx 1$. Using this reference starting point, the experimental conditions (T), and material properties (μ, $L^\star$), we predict G_{cut} *versus* R as shown in Fig. 7b which aligns with the earlier presentation of the experimental results in Fig. 2a. As noted previously, the more neo-Hookean Sol-1 : 1 exhibits a higher sensitivity to blade radius with a logarithmic slope of $n_{\mathrm{FE}} = 0.48$ within the experimentally available radius range $R/L^\star \sim 1$–2 and is nearly identical to the experimentally-observed value $n_{\mathrm{stiff}} = 0.53$ (Fig. 7b, light blue dotted lines). Similarly, the Sol-4 : 1 slope predicted by FE is lower and very close to the experimentally-observed value, $n_{\mathrm{FE}} = 0.27$ *versus* $n_{\mathrm{stiff}} = 0.34$ for $R/L^\star \sim 1$–3, respectively (Fig. 7b, dark blue dotted lines). For comparison, we include the experimental cutting energy data (circles). Only the Sol-4 : 1 data are shifted to 'fit' the FE simulations by modifying $L^\star$ by $\approx 0.9L^\star$. This order-one shift factor has no effect on the power-law dependence of the experimental data, it simply shifts the points right. This small discrepancy between FEA and experimental results may be due to a lack of precision in $L^\star$, which is limited to some extent by the blade radius values available.

To provide further physical insight into the evolution of $V_{\min}$ with increasing force and radius, we visualize and compare the FE near-tip deformation fields of the two materials in Fig. 7d and e. The images correspond to a close-up of the deformation near the tip of the needle as indicated by the insets in Fig. 7c. In the left-most image of each panel, a blade of radius $R/L^\star = 1$ applies F^*_{cut} sufficient to attain $V_{\min}$ using each material's respective threshold strain energy density cutoff w_t/μ. When the blade radius is tripled, $R/L^\star = 3$, the same force is no longer capable of producing such a large damage volume (red region). Only with increasing force is $V_{\min}$ eventually attained at which point we predict steady-state cutting to progress (fourth image in the series). From the shape of the deformed damage zones, it is clear that the more neo-Hookean, Sol-1 : 1-like material more readily deforms to accommodate the blade. The necessary cutting force to maintain $V_{\min}$ at the increased radius $3R$ as depicted in last of these images comes from Fig. 7a. The $F/(\mu R)$ value at $R/L^\star = 3$ is determined from the x-coordinate corresponding to $V/(R^2t) = V_{\min}/[(3L^\star)^2t] = 4/9$ *via* interpolation. We indicate the position of the large blade radius threshold values in both Fig. 7a and b using light-colored solid squares and a star or triangle to indicate correspondence with the Sol-4 : 1 or Sol-1 : 1 like material, respectively. The Sol-1 : 1 like material requires a cutting force $\approx 2.0F^*_{\mathrm{cut}}$ to achieve $V_{\min}$ at $R/L^\star = 3$, while the Sol-4 : 1 like material only requires $\approx 1.8F^*_{\mathrm{cut}}$.

We conclude that for highly elastic materials under small-scale-yield-like conditions, *i.e.*, in which a dissipation zone $\sim \ell_{\mathrm{d}}$ is small and thus contributes little to the observed response, the effective cutting energy is entirely governed by the ability to achieve a threshold damage zone size $\sim \ell^\star$ of the order determined by the blade radius at the onset of the cutting threshold $L^\star$. The use of a blade radius above the threshold length scale reduces the ability of the applied cutting force to achieve the minimum damage zone size. The reduction in effectiveness depends on the deformability of the material being cut, with materials exhibiting a more neo-Hookean response requiring more force and thus being more resistant to cutting. These ideas are consistent with the cutting–tearing equivalence parameter used to quantitatively link cutting and tearing energies.

4.4 A BPDMS case study

We designed a series of four BPDMS elastomers (Section 2.1) as a case study to probe the onset the cutting threshold $L^\star$. An important initial consideration for this series of materials was that their constitutive response prior to failure match since the nonlinear response was known to play a role in the sensitivity of G_{cut} to radius outside of the threshold regime. Our initial aim was to decouple the values of $L^\star$ and n_{stiff}, and thus, a set of unimodal materials having different chain lengths N_x was insufficient since a variable N_x alters the stress–strain response. However, our hope of tuning $L^\star$ using the series of BPDMS elastomers did not produce the anticipated results. Instead our results suggest several interesting avenues for future inquiry.

First, all BPDMS formulations have a nearly linear response while still exhibiting finite deformation (Fig. 2d). Such linear responses may be a compromise between a highly strain stiffening response that leads to a higher G_{tear} than G_{cut} and a primarily neo-Hookean response that leads to the reverse. BPDMS formulations fall closest to direct correspondence between cutting and tearing, exhibiting an equivalency factor of $\mathscr{E}_{\mathrm{CT}}$ = 0.14 to 0.2 for all but the stretchiest 90s formulation ($\mathscr{E}_{\mathrm{CT}}$ = 0.25). It may be that this range of equivalency factors provides an optimum for elastic materials aiming to be equally resistant to both cutting and tearing failure. Given eqn (3), a material that is equally resistant to cutting and tearing would exhibit an $\mathscr{E}_{\mathrm{CT}} = 1/\alpha = 0.14$, which is close to the range of BPDMS values and also consistent with the $\mathscr{E}_{\mathrm{CT}}$ observed for Syl-10 : 1, which gives the best combination of tearing and cutting resistance of all of the materials tested.

Second, the length scales at the onset of the threshold L^* for the BPDMS samples are not significantly different than those obtained for the multi-modal commercial networks. Nor do they differ from one another in a systematic way as one might expect from the variation in long-chain length for each formulation. We believe this may be due in part to resolution limitations of the Y-shaped cutting technique. In the region in which these transitions occur, ≈100–150 nm, we are limited by available razor blade radii. To our knowledge and based on our measurements, only the utility razor blade falls within this range ($R \approx 129$ nm) and it is challenging to precisely alter the radius through manual blunting. Thus we are unable to make any conclusive claims about a change in L^* for the BPDMS samples as originally hoped. However, the marked increase in L^* for BPDMS relative to the unimodal network (Fig. 2a and Table 2) indicates that the damage zone is greatly enlarged by this single change in microstructure, to an extent that far outpaces an increase in average network mesh size.

Two potential microstructural changes may be responsible for the expanded damage zone: effective coordination number and disorder in available chain lengths. Based on previous literature,[46–50] it seems likely that for the highest short-chain concentrations (90s, 95s, and 98s), BPDMS exhibits significant kinetically induced short-chain clustering. These 'super-crosslink' structures are linked together by long-chain lengths of 17 200 g mol^{-1}, 28 000 g mol^{-1}, and 43 000 g mol^{-1}, respectively (Table 1). For these formulations, the strain at break increases with decreasing short chain concentration. This trend reverses for 80s, the next available formulation given limitations in commercially available long-chains. At this lower short-chain concentration, previous work suggests the kinetically-induced clustering becomes less significant and the enhancement in ultimate properties vanishes.[47,50] For the potentially short-chain-clustered microstructures, any super-crosslink network would possess an effectively larger coordination number for the long-chains which would serve as the primary deformable network. Even without this increased coordination number, all formulations possess a level of disorder in available chain lengths due to their bimodal distribution. Such disorder effectively engages two different length scales when a linkage contains both short and long chains. Both high coordination number and hierarchical linkage mechanisms appear sufficient to increase the critical size of the near crack tip regime contributing to failure L^*, consistent with previous theoretical predictions.[38,51] Future work more directly controlling network structure may provide the ability to control L^* and could lead to an approach to increase it. The latter would be expected to improve a material's failure properties.

5 Conclusions

This work looks at the cutting response of highly elastic silicones and their failure response under more blunted loading conditions, including blades of increasing radius and far-field tearing. We demonstrate that when cracks are blunted, the attainment of local damage criteria are mitigated by the non-linear constitutive response of the material. We provide evidence of a threshold damage zone necessary for failure that extends beyond the molecular plane postulated by Lake & Thomas.[32] We emphasize that though cohesive bond failure may also occur outside of this damage zone, it is the cohesive failure within the damage zone that directly facilitates new surface creation. The quantitative effectiveness of a new dimensionless group, the cutting–tearing equivalency parameter, and finite element simulation of blade radius-dependent indentation, demonstrate that achieving this damage zone depends on the deformability of the material. For example, more highly-deformable materials stretch easily around a blade of increasing radius and thus require more force to activate the threshold volume required for the damage zone. These two components of failure are represented in the new dimensionless parameter, which combines both the ultimate failure properties and its nonlinear response. Using the cutting–tearing equivalency parameter we quantitatively map, for the first time, cutting energies to tearing energies.

Our findings suggest a new direction in the search for failure criteria in highly elastic soft solids. First, a critical, threshold damage volume and strain energy density might be determined, *e.g.*, using Y-shaped cutting to find the onset of the threshold cutting response. The onset length scale and threshold energy would then guide the choice of failure criteria in finite element software. Like the simulations for blunted blades, failure occurs when the net volume of the elements meeting or exceeding the threshold strain energy density exceeds $\sim L^{*2}t$. Open questions remain as to the role of sample thickness (all tests were performed in plane stress) and the exact dimensions of the damage zone (we have assumed $V = (2L^*)^2t$ here). Nevertheless, we believe this work has provided a quantitative experimental-evidence-driven approach toward establishing numerically implemented fracture criteria for soft solids.

Conflicts of interest

There are no conflicts to declare.

Acknowledgements

This material is based upon work supported by the National Science Foundation under Grant No. 1562766.

Notes and references

1 G. J. Lake and O. H. Yeoh, *Int. J. Fract.*, 1978, **14**, 509–526.
2 A. N. Gent, S. M. Lai, C. Nah and C. Wang, *Rubber Chem. Technol.*, 1994, **67**, 610–618.
3 A. N. Gent, *Langmuir*, 1996, **12**, 4492–4495.
4 B. Zhang, C. S. Shiang, S. J. Yang and S. B. Hutchens, *Exp. Mech.*, 2019, 517–529.
5 C. T. McCarthy, A. N. Annaidh and M. D. Gilchrist, *Eng. Fract. Mech.*, 2010, **77**, 437–451.
6 P. Han, D. Che, K. Pallav and K. Ehmann, *Int. J. Mech. Sci.*, 2012, **65**, 157–167.
7 S. Mzabi, D. Berghezan, S. Roux, F. Hild and C. Creton, *J. Polym. Sci., Part B: Polym. Phys.*, 2011, **49**, 1518–1524.
8 C. Creton and M. Ciccotti, *Rep. Prog. Phys.*, 2016, **79**, 046601.
9 R. Long, C. Y. Hui, J. P. Gong and E. Bouchbinder, *Annu. Rev. Condens. Matter Phys.*, 2021, 71–94.
10 C. Chen, Z. Wang and Z. Suo, *Extreme Mech. Lett.*, 2017, **10**, 50–57.
11 J. M. Clough, C. Creton, S. L. Craig and R. P. Sijbesma, *Adv. Funct. Mater.*, 2016, **26**, 9063–9074.
12 R. Long and C. Y. Hui, *Soft Matter*, 2016, **12**, 8069–8086.
13 C.-Y. Hui, A. Jagota, S. J. Bennison and J. D. Londono, *Proc. R. Soc. A*, 2003, **459**, 1489–1516.
14 R. Bai, J. Yang and Z. Suo, *Eur. J. Mech., A*, 2019, **74**, 337–370.
15 Y. Zhou, J. Hu, P. Zhao, W. Zhang, Z. Suo and T. Lu, *J. Mech. Phys. Solids*, 2021, 104483.
16 J.-Y. Sun, X. Zhao, W. R. K. Illeperuma, O. Chaudhuri, K. H. Oh, D. J. Mooney, J. J. Vlassak and Z. Suo, *Nature*, 2012, **489**, 133–136.
17 F. J. Massey Jr, *J. Am. Stat. Assoc.*, 1951, **46**, 68–78.
18 E. M. Arruda and M. C. Boyce, *J. Mech. Phys. Solids*, 1993, **41**, 389–412.
19 M. C. Boyce, *Rubber Chem. Technol.*, 1996, **69**, 781–785.
20 A. Spagnoli, M. Terzano, R. Brighenti, F. Artoni and P. Ståhle, *Int. J. Mech. Sci.*, 2018, **148**, 554–564.
21 V. R. Krishnan, C. Y. Hui and R. Long, *Langmuir*, 2008, **24**, 14245–14253.
22 E. Bouchbinder, A. Livne and J. Fineberg, *J. Mech. Phys. Solids*, 2009, **57**, 1568–1577.
23 R. Long and C. Y. Hui, *Extreme Mech. Lett.*, 2015, **4**, 131–155.
24 T. T. Mai, K. Okuno, K. Tsunoda and K. Urayama, *ACS Macro Lett.*, 2020, **9**, 762–768.
25 T. Chanthasopeephan, J. P. Desai and A. C. Lau, *IEEE Trans. Biomed. Eng.*, 2007, **54**, 349–359.
26 M. Oldfield, D. Dini, G. Giordano and F. Rodriguez y Baena, *Comput. Methods Biomech. Biomed. Eng.*, 2013, **16**, 530–543.
27 M. Gzaiel, E. Triki and A. Barkaoui, *Mech. Mater.*, 2019, **136**, 103082.
28 B. Takabi and B. L. Tai, *Med. Eng. Phys.*, 2017, **45**, 1–14.
29 A. Leibinger, M. J. Oldfield and F. Rodriguez y Baena, *Interface Focus*, 2016, **6**, 1–10.
30 K. Mansouri, M. Arfaoui, M. Trifa, H. Hassis and Y. Renard, *Int. J. Solids Struct.*, 2016, **80**, 532–544.
31 V. M. Mal'kov and Y. V. Mal'kova, *J. Appl. Math. Mech.*, 2008, **72**, 468–474.
32 G. J. Lake and A. G. Thomas, *Proc. R. Soc. London, Ser. A*, 1967, **300**, 108–119.
33 R. S. Rivlin and A. G. Thomas, *J. Polym. Sci.*, 1953, **10**, 291–318.
34 T. Atkins, *The Science and Engineering of Cutting*, Elsevier, 2009, ch. 9, pp. 221–243.
35 R. Pourmodheji, S. Qu and H. Yu, *J. Appl. Mech.*, 2019, **86**, 1–11.
36 M. F. Ashby, *Materials Selection in Mechanical Design*, Elsevier, 4th edn, 2011, pp. 125–195.
37 K. Y. Volokh, *Mater. Theory*, 2017, **1**, 3.
38 S. Lin and X. Zhao, *Phys. Rev. E*, 2020, **102**, 52503.
39 J. Slootman, V. Waltz, C. J. Yeh, C. Baumann, R. Göstl, J. Comtet and C. Creton, *Phys. Rev. X*, 2020, **10**, 41045.
40 M. Rubinstein and S. Panyukov, *Macromolecules*, 2002, **35**, 6670–6686.
41 A. C. M. Kuo, *Polymer Data Handbook*, Oxford University Press, Inc., 1999, pp. 411–435.
42 S. Wang, S. Panyukov, M. Rubinstein and S. L. Craig, *Macromolecules*, 2019, **52**, 2772–2777.
43 M. I. Giannotti and G. J. Vancso, *ChemPhysChem*, 2007, **8**, 2290–2307.
44 M. K. Beyer, *J. Chem. Phys.*, 2000, **112**, 7307–7312.
45 S. Al-Maawali, J. E. Bemis, B. B. Akhremitchev, R. Leecharoen, B. G. Janesko and G. C. Walker, *J. Phys. Chem. B*, 2001, **105**, 3965–3971.
46 B. D. Viers and J. E. Mark, *J. Macromol. Sci., Part A: Pure Appl. Chem.*, 2007, **44**, 131–138.
47 F. B. Madsen, A. E. Daugaard, C. Fleury, S. Hvilsted and A. L. Skov, *RSC Adv.*, 2014, **4**, 6939–6945.
48 W. Michalke, S. Kreitmeier, M. Lang, A. Buchner and D. Göritz, *Comput. Theor. Polym. Sci.*, 2001, **11**, 459–466.
49 H. Oikawa, *Polymer*, 1992, **33**, 1116–1119.
50 G. D. Genesky, B. M. Aguilera-Mercado, D. M. Bhawe, F. A. Escobedo and C. Cohen, *Macromolecules*, 2008, **41**, 8231–8241.
51 K. Kothari, Y. Hu, S. Gupta and A. Elbanna, *J. Appl. Mech.*, 2018, **85**, 1–11.